Title

Diffusive confinement of free radical intermediates in the OH radical oxidation of semisolid aerosols

Journal

Physical Chemistry Chemical Physics, 19(9)

ISSN

1463-9076

Authors

Wiegel, Aaron A
Liu, Matthew J
Hinsberg, William D
et al.

Publication Date

2017-03-01

DOI

10.1039/c7cp00696a

Peer reviewed

Diffusive Confinement of Free Radical Intermediates in the OH Radical Oxidation of Semisolid Aerosol

Aaron A. Wiegel,[a] Matthew J. Liu,[a,b], William D. Hinsberg,[c] Kevin R. Wilson,[*a] and Frances A. Houle[*a]

[a]*Lawrence Berkeley National Laboratory, Chemical Sciences Division, Berkeley, CA, USA 94702*

[b]*University of California, Berkeley, Department of Chemical and Biomolecular Engineering, Berkeley, CA, USA 94702*

[c]*Columbia Hill Technical Consulting, Fremont, CA, USA 94539*

*To whom correspondence should be addressed. Email: fahoule@lbl.gov (510-495-8135) or krwilson@lbl.gov (510-495-2474)

†Electronic Supplementary Information (ESI) available: [details of any supplementary information available should be included here]. See DOI: 10.1039/x0xx00000x

Abstract

Multiphase chemical reactions (gas+solid/liquid) involve a complex interplay between bulk and interface chemistry, diffusion, evaporation, and condensation. Reactions of atmospheric aerosols are an important example of this type of chemistry: the rich array of particle phase states and multiphase transformation pathways produce diverse but poorly understood interactions between chemistry and transport. Their chemistry is of intrinsic interest because of their role in controlling climate. Their characteristics also make them useful models for study of principles of reactivity of condensed materials under confined conditions. In previous work, we have reported a computational study of the oxidation chemistry of a liquid aliphatic aerosol. In this study, we extend the calculations to investigate nearly the same reactions at a semisolid gas-aerosol interface. A reaction-diffusion model for heterogeneous oxidation of triacontane by hydroxyl radicals (OH) is described, and its predictions are compared to measurements of aerosol size and composition, which evolve continuously during oxidation. These results are also

explicitly compared to those obtained for the corresponding liquid system, squalane, to pinpoint salient elements controlling reactivity. The diffusive confinement of the free radical intermediates at the interface results in enhanced importance of a few specific chemical processes such as the involvement of aldehydes in fragmentation and evaporation, and a significant role of radical-radical reactions in product formation. The simulations show that under typical laboratory conditions semisolid aerosols have highly oxidized nanometer-scale interfaces that encapsulate an unreacted core and may confer distinct optical properties and enhanced hygroscopicity. This highly oxidized layer dynamically evolves with reaction, which we propose to result in plasticization. The validated model is used to predict chemistry under atmospheric conditions, where the OH radical concentration is much lower. The oxidation reactions are more strongly influenced by diffusion in the particle, resulting in a more liquid-like character.

I. Introduction

Although submicron-scale organic atmospheric aerosol are immensely complex chemical mixtures, in-depth investigations of the chemistry of single-component systems under well-controlled conditions as models provide important insights to how aerosol particles transform in their natural environment. Studies that couple experiments with detailed kinetics models are particularly valuable since the resulting predictive description can both elucidate the reaction-diffusion mechanisms involved and inform comprehensive climate models. There is an important body of work directed toward this end, with particular emphasis on finding useful descriptions of transport for reacting aerosol systems. The fundamental questions being addressed concern how the aerosol phase state influences gas-particle partitioning and how motion of reactants and products within the aerosol particle influence the particle properties and any chemical reactions that take place. This has required innovation in computational methods, progressing from simple[1-4] to detailed[5, 6] descriptions of coupled reaction-diffusion processes. Because of the focus on transport, the resulting chemical reactions are treated in less detail and describe mainly the first reaction generation, for example addition of one oxygen functionality to the organic component of the aerosol.[1-3, 5] Incorporation of multigenerational descriptions of the chemistry relevant to greater extents of reaction is a complex process, particularly when extended free radical chain reactions are involved. Successful approaches include some degree of lumping of related chemistries[7, 8] and treatment of reacting molecules as systems of functionalities rather than distinct species.[9] The core challenge to incorporation of chemistry in full is the paucity of validated measurements of detailed interfacial and condensed phase free radical kinetics for the full

scope of compounds typically present in aerosol. Rate coefficients for reaction, adsorption, and transport can be discovered by global fits of large data sets using a representative reaction scheme, [10, 11] or estimated using theory or quantitative comparison to experiment for cases where most but not all of the coefficients have been measured and validated in separate studies.[6, 9] Incorporation of known microscopic rate coefficients is crucial when the aim of the work is to find fully predictive models for use in new systems as well as gain new understanding of the specific system under study.

Single component aerosol chemistry has deeper intrinsic interest, however. Because aerosol particles are objects with well-defined properties, their study can reveal general concepts of reactivity characteristic of nanoscale environments. Recent studies have shown that chemistry in confined spaces such as droplets, emulsions, and micelles[12-18] can differ in important ways from chemistry in a semi-infinite bulk environment because the interfaces between an external condensed phase and the reacting system influence the local organization of the molecules. Organic aerosol particles are an excellent system to explore these concepts: their surfaces are only in contact with the gas phase, which eliminates the possibility that another condensed system participates in the chemical reactions involved, and the aerosol composition and internal molecular mobility can be varied independently. Moreover the interface to a gas ensures free transfer of chemical species into and out of the reacting volume so that regimes of chemical and transport control of the reaction rates can be distinguished. This level of control over the properties of the reactive environment under study enables the factors that most strongly influence the chemical mechanism to be disentangled.

Organic aerosol reacting with OH, a model for atmospheric aging, is a chemical system particularly well suited to investigate these concepts. Oxidation continuously transforms organic aerosol over their 5-10 day lifetime after formation.[19] These particles can have a range of viscosities spanning liquid to semi-solid,[20-24] which influences the uptake and reaction rates of gas-phase oxidants such as OH radicals or O_3,[6, 25-27] evaporation of small molecules from the aerosol surface,[20, 22] and uptake of water as the aerosol becomes more hydrophilic.[28] To investigate the influence of viscosity (mobility) on aerosol reactivity, we have used the oxidation of 30-carbon aliphatic alkane chains by OH as a class of model systems. OH-alkane chemistry involves extensive free radical chain reactions launched by abstraction of H from the molecules present in the particle.[9, 29] By constructing a detailed reaction-diffusion kinetics scheme and validating it using diverse data from experimental measurements on two different alkanes, we can identify mechanistic details that control reactivity in these systems and predict phenomena beyond the original observations with some confidence. Models in which the rate coefficients are determined as fitting parameters for an assumed scheme are less useful for this purpose.

In a previous study, we have described a kinetics model for OH reacting with squalane, a liquid C_{30} molecule (squalane) that is well-mixed under the experimental conditions used.[9] The particle was treated as a single volume, which has been shown to yield the same results as full reaction-diffusion[6] and simplified the scheme considerably. A semi-detailed reaction scheme was introduced that treated the molecules and free radical intermediates as a collection of functional groups and carbon backbones rather than explicitly treating each possible species.[9] This approach is similar to that used in a

114 previous model of gas phase free radical chemistry[30, 31] and polymer dissolution
115 simulations.[32] The calculations identified key free radical reactions that lead to
116 functionalization, fragmentation, and particle mass loss. The simulations successfully
117 predicted the evolution of aerosol mass, volume, elemental composition, and carbon
118 fragment distribution over ten oxidation lifetimes (i.e., when the average squalane
119 molecule has been oxidized ten times by OH radicals). It was found that alkoxy radicals
120 activated by adjacent oxygen functional groups[33] are primarily responsible for generation
121 of fragmentation products as the aerosol becomes progressively more oxidized. Their
122 formation is an essential element influencing the reactivity in this liquid, well-mixed
123 system.[19, 34]

124 We have also examined OH uptake, which measures the consumption of reactants
125 per OH-particle collision.[6] The simulations showed that this process does not depend on
126 the details of the free radical chemistry alone, but rather, it is an emergent process
127 depending also on the aerosol size and on the internal mobility (viscosity) of the
128 molecules in the aerosol relative to the OH reaction frequency. This result is general,
129 indicating that reactivity is dependent on the details of gas-surface interactions in a more
130 complex way than would be anticipated from studies of gas-liquid reactions.[35, 36]

131 In the present work, we examine the influence of greatly reduced internal mobility
132 while keeping the chemistry essentially the same. We model the reaction of OH with a
133 semi-solid aerosol, triacontane, an isomer of squalane, using the semi-detailed kinetic
134 scheme developed for squalane.[9] The scheme has been extended to include more
135 extensive oxidation, and full internal diffusion has been incorporated using the
136 description presented previously in OH uptake kinetics simulations.[6] The simulated mass

and elemental compositions of the triacontane aerosol particle as a function of OH exposure are in good agreement with previously published measurements.[19, 29, 34, 37] The simulations reveal details about the radial distribution of heterogeneous oxidation products in a semisolid organic aerosol. Such inhomogeneities were proposed to explain results of an experimental study of brassidic acid oxidation,[38] but their details are currently inaccessible by experiment. A quantitative description of them through detailed modeling provides important information for representing aerosols in atmospheric models. The simulations also provide new insights into how viscosity influences reactivity in the aliphatic hydrocarbon – OH system including the effect of diffusive confinement of the chemistry in the outer surface layers of the particle, the resulting dominance of specific branches of the chemistry, and how some branches suppress and others activate fragmentation.

The paper is organized as follows. We describe how the reaction-diffusion model has been developed using previous work on squalane as a starting point. Extensive details are presented in the Electronic Supplementary Information (ESI†) section. Because of the lack of experimental or theoretical information on several mechanistic elements we have performed scenario calculations and compared them to experimental data to identify appropriate quantitative ranges. Finally, simulation results are presented and discussed in terms of their atmospheric chemistry implications and, taken together with the liquid squalane oxidation results, what they reveal about how viscosity controls reactivity under confined conditions.

II. Model Development

160 *A. Simulation Overview*

161 A reaction-diffusion kinetic model was developed using *Kinetiscope*.[39] This open
162 access software package (http://hinsberg.net/kinetiscope/) does not integrate coupled
163 differential equations, but rather uses stochastic algorithms, originally developed by
164 Bunker[40] and Gillespie,[41] to propagate a reaction. The method provides a solution to the
165 master equation for a reaction-diffusion system. When used with elementary rate
166 constants for individual chemical steps, these calculations produce an absolute time base
167 and predictions that can be validated by direct comparison to experiment. This method
168 has been significantly extended for modeling complex reaction-diffusion phenomena[32, 42-
169 44] that would be difficult or nearly impossible to simulate using conventional integrators,
170 *e.g.*, stiff systems (i.e., simultaneous, very fast and very slow processes), processes that
171 depend on sporadic events such as nucleation or explosions, or processes such as
172 evaporation and density changes that dynamically alter volumes. As described in detail in
173 those studies, the simulation methodology used in the present work for Type I (Fickian)
174 and Type II (non-Fickian) diffusion has been rigorously validated and demonstrated to be
175 fully predictive. The application of this approach to aerosol chemistry can be found in
176 subsequent publications.[6, 9]

177 Development of the core aliphatic organic oxidation mechanism[9] was performed
178 for squalane using a single compartment as the reaction volume. Because internal mixing
179 was very fast compared to experiment this is a realistic representation. Extension to more
180 viscous systems requires full inclusion of diffusion throughout the particle. The generic
181 simulation framework used is summarized below and in Fig 1. A single aerosol particle is
182 represented by a stack of Cartesian compartments. The compartments are connected in a

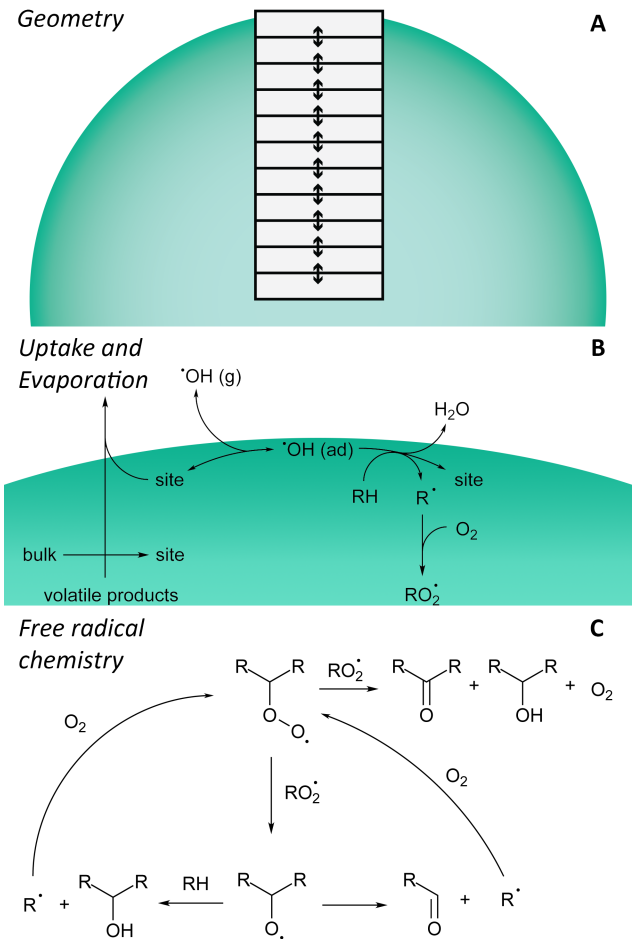

Figure 1. Overview of the three main components used to simulate the heterogeneous oxidation of organic aerosol. (A) The spherical aerosol is treated as a stack of radial Cartesian compartments that can shrink or grow as material becomes more or less dense through chemical reactions or enters and leaves the compartment through diffusion, evaporation, or condensation. Fickian diffusion is allowed between each adjacent compartment as represented by the double-headed arrows. (B) In the top compartment, gas phase OH radicals adsorb, desorb or react with organic materials (RH) to eventually yield organic peroxy radicals (RO_2). Volatile organic fragments formed from the free radical chemistry can evaporate. (C) The RO_2 react with other RO_2 radicals to form a ketone and an alcohol or two alkoxy (RO) radicals. The RO radicals can abstract a hydrogen, which forms an alcohol and promotes free radical cycling, or fragment via β scission to form more volatile, lower molecular mass products.

continuous radial core through the aerosol extending from the center of the particle to its outer surface, as shown in Fig. 1A. For example, to simulate an aerosol with a radius of

199 54.5 nm, we used a stack of 109 individual 13.17 × 13.17 nm compartments that are 0.5
200 nm thick. Larger particle sizes are simulated by simply adding more compartments.
201 Additional details can be found in the ESI Sec. S1†.
202
203 The outermost compartment represents the gas-particle surface and contains
204 additional multiphase pathways the exchange of material to and from the gas phase
205 (uptake and evaporation) as shown in Fig. 1B. The compartments beneath the surface
206 represented the bulk regions of the aerosol. Species (i.e. molecules) move between
207 compartments via diffusion pathways shown schematically as arrows in Fig. 1A. Because
208 of the difference in geometry between the stack of compartments and the spherical
209 aerosol, a correction is applied to the calculated concentrations resulting from the
210 simulations by using an equivalent spherical shell to properly weight the contributions
211 from each subvolume. This allows the simulation results to be compared directly to
212 experiment.
213 Within each compartment, elementary reaction steps describe the
214 multigenerational reaction of OH with triacontane. Formulating a reaction scheme
215 explicitly by specifying individual reaction steps for all possible isomers at each
216 generation of oxidation would require delineating thousands of elementary reactions
217 between thousands of individual products and intermediates.[7,9] In the semi-detailed
218 representation, a more tractable alternative, a molecule is represented as a collection of
219 reactive hydrogen atom sites. Thus, triacontane ($C_{30}H_{62}$), a linear alkane, is represented as
220 two methyl groups (CH_3) and twenty-eight methylene groups (CH_2) on a 30-carbon
221 skeleton. As OH radicals react with triacontane, the CH_3 and CH_2 functional groups are

converted into free radical intermediates and eventually into stable functional group products such as ketones or alcohols (described below). C-C bond scission (fragmentation) reactions are represented by randomly splitting the original C_{30} backbone into two smaller carbon numbered products (such as C_{27} and C_3). This compact description enables predictions of elemental composition and aerosol mass as a function of OH exposure, which can be quantitatively compared to experimental measurements.

The rate of gradient-driven diffusion between compartments is defined according to Fick's law. Diffusion is only allowed to occur by exchange--that is, only when there is a free volume space is available in the adjacent compartment, analogous to the classic model of Cohen and Turnbull.[45] The self-diffusion coefficient used for triacontane is 8.3 $\times$ 10^{-19} cm^2 s^{-1}. This value is derived from the zero-shear limit of measurements of the dynamic viscosity (see ESI Sec. S7†). The diffusion coefficient is initially assumed to be Type I, i.e. constant for each functional group and carbon backbone as triacontane is oxidized, but this assumption is explicitly tested as discussed below.

Finally as material diffuses, evaporates or reacts to form products of different densities, the individual compartments are allowed to expand or contract independently in three dimensions as described elsewhere[43] with the smaller of the 2 areas at the interface between two compartments chosen to be the area of the interface. In this way, the simulated size of the aerosol evolves dynamically with oxidation, and the concentrations are continuously corrected so that the diffusion and reaction rates are accurate.[43]

B. Detailed Reaction Mechanism

The goal of this work is to describe accurately the multigenerational heterogeneous chemistry of OH reacting with triacontane. Our starting point is the basic reaction free radical oxidation scheme developed previously[9] and shown schematically in R1-R4 (Fig. 1C),

$$OH + RH \rightarrow R + H_2O \quad (R1)$$

$$R + O_2 \rightarrow RO_2 \quad (R2)$$

$$RO_2 + RO_2 \rightarrow \textit{Ketone and Alcohol} + O_2 \quad (R3)$$

$$RO_2 + RO_2 \rightarrow 2RO + O_2 \quad (R4)$$

OH abstracts a hydrogen atom (R1) from a C-H bond (RH) on a hydrocarbon or partly oxidized product to form an alkyl radical (R) and H_2O. In the presence of O_2, R is rapidly converted to a peroxy radical (RO_2, R2) whose subsequent reaction pathways form stable alcohol and ketone products (R3) or two alkoxy radicals (RO, R4). Rate coefficients used for R1-R4 are constrained to previous literature values as shown in Table 1.

Additional reaction steps are needed to simulate the oxidation of a semisolid aerosol like triacontane. In particular, carboxylic acids are products of the heterogeneous oxidation of viscous n-alkanes[46] but not liquid ones, so new mechanistic pathways are required to describe their formation and fragmentation reactions.

Table 1. Summary of simulation parameters used to predict the heterogeneous oxidation of triacontane by OH radicals. References for literature values are included in the table.

Parameter	Description	Value

d_p	Diameter of particle	109 or 145 nm[a]
ρ_0	Density of particle	0.81 g cm^{-3}
k_{ad}	Pseudo-first order adsorption rate coefficient of OH	10 s^{-1}
k_{des}	Desorption rate coefficient of OH[47]	2.86×10^{10} s^{-1}
k_{Tri+OH}	Total rate coefficient for OH + triacontane[48]	1.55×10^{-11} cm^3 $molecules^{-1}$ s^{-1}
$k_{CH3\text{-}s}$	Rate coefficient of OH + surface-aligned CH_3[46, 48, 49]	8.69×10^{-13} cm^3 $molecules^{-1}$ s^{-1}
k_{CH3}	Rate coefficient of OH + bulk CH_3[46, 48, 49]	4.35×10^{-14} cm^3 $molecules^{-1}$ s^{-1}
$k_{CH2\text{-}\alpha}$	Rate coefficient of OH + surface aligned CH_2[46, 48, 49]	2.90×10^{-12} cm^3 $molecules^{-1}$ s^{-1}
k_{CH2}	Rate coefficient of OH + bulk CH_2[46, 48, 49]	4.35×10^{-13} cm^3 $molecules^{-1}$ s^{-1}
$k_{RO2+RO2}$	Rate coefficient of RO_2 + RO_2[50]	1.61×10^{-15} cm^3 $molecules^{-1}$ s^{-1}
$k_{RO2+R(O)O2}$	Rate coefficient of RO_2 + $R(O)O_2$[50]	1.61×10^{-15} cm^3 $molecules^{-1}$ s^{-1}
k_{RO+RH}	Rate coefficient of RO + RH (alkoxy abstraction) [50]	1.66×10^{-15} cm^3 $molecules^{-1}$ s^{-1}
D_{tria}	Self-diffusion coefficient for triacontane (this work)	8.3×10^{-19} cm^2 s^{-1}
D_{OH}	Diffusion coefficient for OH (based on H_2O diffusion)[28]	10^{-11} cm^2 s^{-1}

[a] Experiments that measured the decay of triacontane (see Fig. 4) used slightly larger sized particles (d_p = 145 nm) than those experiments that measured elemental composition and aerosol mass (Figs. 5-8); d_p = 109 nm. The simulation geometry was modified to accurately simulate the particle size used in each experiment.

273 *Functionalization Reactions.* As the aerosol becomes oxidized, RO_2 + RO_2
274 reactions (R4) will increasingly involve reactions between peroxy radicals with existing
275 oxygenated functional groups (not explicitly shown in R1-R4). For example, acyl peroxy
276 radicals ($R(O)O_2$) were formed from hydrogen abstraction from aldehydes or by β-
277 scission of an alkoxy radical with an adjacent ketone functional group. In the squalane
278 oxidation simulations,[9] the $R(O)O_2$ intermediate was formed only in very small
279 quantities, consistent with the fact that acids are not observed experimentally, and its
280 subsequent reactions were neglected. For triacontane, they reach much higher
281 concentrations due to low diffusivity and must be included. Additional reaction steps are
282 needed to simulate the oxidation of a semisolid aerosol like triacontane. We have added
283 cross reactions between ($R(O)O_2$) and RO_2 radicals to form acyloxy (R(O)O) and RO
284 radicals or carboxylic acids and ketones[51] as shown in Fig. 2. Only a limited number of
285 measurements of cross reactions between $R(O)O_2$ and RO_2 radicals are available in the
286 literature[51, 52] even for the gas phase, and none are available (to our knowledge) in the
287 condensed phase. The branching ratio between the radical and acid formation pathways
288 shown in Fig. 2 are initially set at 90% acid formation (i.e., same as the RO_2 + RO_2
289 branching ratio to form alcohols and ketones, R3). In the reaction scheme, products of the
290 $R(O)O_2$ + $R(O)O_2$ reaction are two R(O)O radicals as observed experimentally.[52]
291

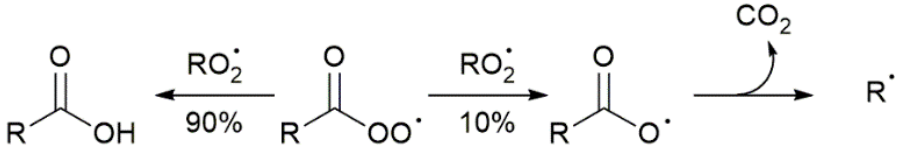

292

293 **Figure 2**. Cross-reactions of acyl peroxy radicals ($R(O)O_2$) with alkyl peroxy (RO_2)
294 radicals. The $R(O)O_2$ radical can either form a carboxylic acid and chain terminate, or an

295 acyloxy (R(O)O) radical which can decompose via CO_2 elimination to form an alkyl
296 radical (chain propagating).
297

298

299 OH radicals can react with carboxylic acids via an abstraction reaction analogous
300 to the aqueous phase reaction observed for oxalic and acetic acid.[53-55] In the absence of
301 literature data, we assumed that the rate coefficient in an organic solvent would be
302 somewhat similar to that in water, although we acknowledge that there are clear
303 differences between reactions in organic and aqueous solvents such as the formation of
304 the more reactive carboxylate ion in the latter. Based on rate coefficients for several
305 carboxylic acids in the aqueous phase, the rate coefficient for the OH abstraction from a
306 carboxylic acid group is chosen to be 10^{-14} molecules cm^3 s^{-1}.[53] OH can also react via
307 addition as has been observed in the gas phase with a rate coefficient of 5.2×10^{-13}
308 molecules cm^3 s^{-1}.[48] Such a reaction could occur near or at the aerosol surface. Given the
309 uncertainty in the dominant kinetics, the sensitivity of the model predictions to the rate
310 coefficient of this step is explicitly tested as described below.

311 HO_2 radicals may in principle react with RO_2 and $R(O)O_2$ to form
312 hydroperoxides, peroxy acids, carboxylic acids, and R(O)O radicals.[56, 57] The importance
313 of this channel was evaluated by including uptake of gas phase HO_2 generated from the
314 reactions of $O(^1D)$ and H_2O in the reactor,[58] and evaporation in the model. Only
315 evaporation of HO_2 is found to be kinetically significant, since the uptake coefficient of
316 HO_2 onto squalane particles[59] is small compared to the large desorption coefficient for
317 HO_2 observed in molecular dynamics (MD) simulations of similar species (OH and O_3).[47]
318 Thus, HO_2 chemistry in this system appears to be insignificant but cannot be entirely

ruled out for other organic aerosol systems, particularly aqueous or metal-containing organic aerosols.[59]

Fragmentation reactions. The loss of aerosol mass in aliphatic oxidation is due to chemical erosion that originates primarily from the formation and subsequent decomposition of activated RO species with an adjacent a ketone or alcohol functional group.[9] The presence of either group enhances the rate of β-scission of alkoxy radicals by 5 orders of magnitude.[9, 33, 60] This fragmentation path for triacontane is extended to include the fragmentation of carbon backbones with less than 30 carbons and to more highly oxygenated reaction products. All possible combinations of fragmentation paths are included as described in ESI Sec S5†. Fragmentation to form CO_2 following abstraction of H from –COOH is also included as shown in Fig. 2.

Whether a carboxylic acid group adjacent to an alkoxy radical site will activate unimolecular decomposition in a manner similar to ketone or alcohol functionalities is unclear from existing literature. Barrier heights for fragmentation of the alkoxy-carboxylic acid moiety are estimated to be 13 kcal mol^{-1} in an organic solvent using GAUSSIAN electronic structure calculations (See ESI Sec. S4† for more details). Using the suggested transition state theory pre-exponential factor A_{TST} of 1.8×10^{13} s^{-1} for 298K,[9, 60] this barrier height results in a fragmentation rate coefficient of 6.96×10^{3} s^{-1}. This value is small compared to that for alkoxy radicals activated by alcohol and ketone groups and suggests that almost all of these carboxylic acid-containing RO radicals will react only via bimolecular hydrogen abstraction reaction. Thus, this decomposition pathway was not included in the reaction scheme.

342 *C. OH Uptake, Surface Orientation and Evaporation*

343 *OH uptake.* OH initiates the reaction as shown in R1, and from previous
344 experimental[61] and computational work,[6] is expected to react mainly in the outermost (1-
345 2 nm) surface layers of the particle (i.e. 2-4 compartments in the squalane simulations).
346 An effective uptake coefficient of OH (γ_{eff}) is computed from experimental
347 measurements by measuring the reactive decay of triacontane in the particle using aerosol
348 mass spectrometry. γ_{eff} is simply the ratio of reactive collisions leading to loss of
349 triacontane to the total number of OH collisions with the aerosol surface. Unlike gas
350 phase measurements of the loss of OH above a surface,[62] γ_{eff} is determined by the
351 consumption rate of a particle phase species and is thus sensitive to both OH reactions as
352 well as reactions with other free radical intermediates that are present (e.g. alkoxy
353 radicals). For cases where large quantities of RO radicals are formed, extensive chain
354 propagation reactions can occur leading to an γ_{eff} larger than 1.[63-65] The observed γ_{eff} for
355 triacontane is less than 1,[64] however as will be discussed below this value is not simple to
356 interpret due to spatial inhomogeneities that lead to large consumption of organic in one
357 region while the average extent of reaction is small.

358 γ_{eff}, obtained by experiment is in reality an aggregate of a number of elementary
359 reactions coupled by diffusion. Reactions R5-R7 are the elementary chemical steps that
360 describe reactive uptake of OH, based upon a theoretical analysis[66] adapted for use in the
361 simulations.[6] Taken together, R5-R7 control the observed consumption of the starting
362 material (i.e., the experimentally observed *effective* reactive uptake of OH, γ_{eff}).

363 $$OH_g + site \xrightarrow{k_{ad}} OH_{ads} \quad \text{(R5)}$$

364 $$OH_{ad} \xrightarrow{k_{des}} OH_g + site \quad \text{(R6)}$$

$$OH_{ad} + RH \xrightarrow{k_{OH+RH}} R + H_2O + site \quad \text{(R7)}$$

These steps describe the following microscopic processes. First, gas phase OH must adsorb (R5) onto a surface site. After adsorption, OH can either desorb (R6) back into the gas phase or react by abstracting a hydrogen atom (R7) from an organic functional group (RH). Thus, the rate coefficients for adsorption (k_{ad}), desorption (k_{des}), and abstraction (k_{OH+RH}) are required inputs for the model.

The desorption rate coefficient (k_{des} in R6) is fixed at 2.86×10^{10} s^{-1} to reflect the 35 ps lifetime of OH on aqueous surfaces observed in MD simulations.[47] The overall rate coefficient for hydrogen abstraction (k_{OH+RH} in R7) is fixed at 1.55×10^{-11} cm^3 $molecule^{-1}$ s^{-1}, which is consistent with previous gas phase rate coefficients for the reaction of OH with long chain alkanes (e.g. tridecane) tabulated by Atkinson.[67]

The adsorption rate coefficient k_{ad} is not known and is therefore adjusted in the simulation to replicate the global data set, which includes the experimental decay of triacontane, elemental composition, and aerosol mass vs. OH exposure observed in two separate experimental studies. Using the experimental average OH concentration of 2.5×10^{11} molecules cm^{-3} a pseudo-first order rate coefficient of $k'_{ad} = k_{ad}[OH] = 10$ s^{-1} is found to best replicate the experimental results. This value corresponds to a second order adsorption rate coefficient of 4×10^{-11} cm^3 $molecules^{-1}$ s^{-1}, which is comparable to the value of 8 x 10^{-11} cm^3 molecules s^{-1} found in the previous reaction-diffusion simulation study of squalane.[6] (The value of 10^{-10} cm^3 molecules s^{-1} reported in that work is corrected for differences in the definitions of sites and compartment geometries between the two studies for comparison purposes). Because of the substantial physical differences between squalane and triacontane particles, the factor of 2 difference in estimated

adsorption coefficients does not have a clear origin, but would be interesting to understand in greater detail.

Surface Orientation. There is evidence that linear n-alkanes, like triacontane, adopt preferred surface orientations sometimes referred to as "surface freezing."[68, 69] Alkanes molecules orient with one terminal methyl group extending away from the gas-surface interface and the other terminal methyl group buried in the interior.[46, 49, 70, 71] To account for this in the model, one methyl group and one methylene group are given special designations to indicate their proximity to the surface. The surface-aligned methyl group is termed CH_3-*s*, while the surface-aligned methylene group is given the label *α* to indicate that it is one carbon away from CH_3-*s*, as shown in Fig. 3.

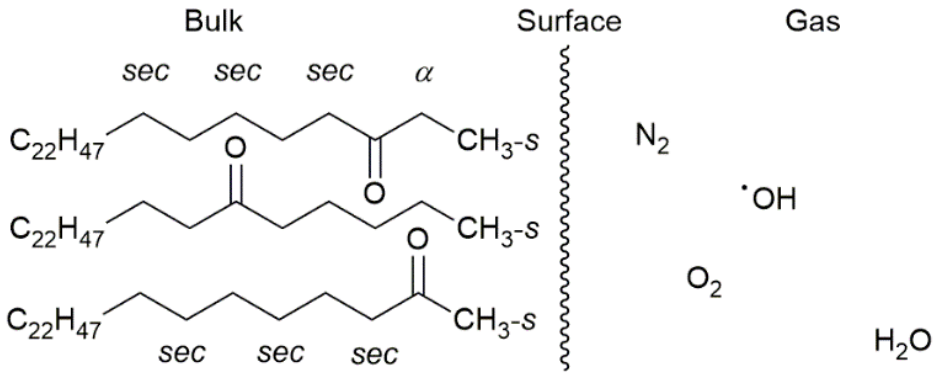

Figure 3. A schematic showing the functional group designations used in the reaction scheme to indicate proximity to the surface. The surface aligned methyl group is CH_3-*s*, the methylene group one carbon away from that methyl group is CH_2-*α*, and all other methylene groups are CH_2-*sec*.

These surface-aligned groups are assumed to have larger OH abstraction rate coefficients since they extend from the surface into the gas phase and preferentially interact with incoming gas phase OH. The hydrogen abstraction rate coefficients are

chosen so that their ratio across the CH_3-*s*, CH_2-*α*, and the CH_2-*bulk* groups are approximately the same as the observed ratios of resulting ketone and alcohol isomers in the oxidation of other linear n-alkanes.[46, 49] Although the abstraction rate coefficient varied with location on the chain, the total overall rate coefficient for hydrogen abstraction from any part of triacontane is maintained at a value of 1.55×10^{-11} cm^3 $molecule^{-1}$ s^{-1} using weighted averaging. This value is assumed to apply even for oxidation of the fragmentation products residing in the surface compartment. The OH abstraction rate coefficients for hydrogen atoms located on the same carbon atom as an existing alcohol or aldehyde functional group are assumed to increase by factors of 3.5 and 8.7, respectively, as predicted by the gas phase structure activity relationships (SAR).[48] Rate coefficients for these hydrogen abstraction reactions and other model parameters are shown in Table 1.

Evaporation. Evaporation rate coefficients have not been measured for this system, so they are instead estimated from vapor pressures found using the group additivity model, EVAPORATION, using the carbon backbone length and the number of primary functional groups (e.g., aldehyde or carboxylic acids).[72] Raoult's Law, the Hertz-Knudsen equation, and the geometry of the particle are then used to estimate rate coefficients for evaporation as described in a previous publication[9] (see Sec. S6† for more details.) For low molecular weight dicarboxylic acids (e.g., succinic acid) the measured vapor pressures are used[73] since group contribution methods are known to overestimate the vapor pressures for this class of compounds.[74] Given the large uncertainties in the estimated vapor pressures, evaporation rate coefficients could in principle be a large source of uncertainty in the model. In practice, however, increasing

431 or decreasing the evaporation rate coefficients by a factor of 10 produces only minor
432 differences in the model predictions as will be discussed below because any increase or
433 decrease in the quantity of lower molecular weight products remaining in the aerosol
434 results in a corresponding decrease or increase in CO_2. The uncertainty in these values
435 will likely matter for more branched organic species or for more liquid-like cases,
436 however.[9]

437 Since each chemical entity in the simulation has an associated carbon backbone
438 length and a functional group volume, changes in aerosol density and size due to
439 evaporation are captured in the simulations. The total volume of a compartment
440 corresponds to the sum of individual functional group partial volumes derived from X-ray
441 diffraction[75] and density measurements. In the simulation, an evaporation step removes
442 the carbon backbone, associated functional group species, and OH adsorption/reaction
443 sites from the compartment, decreasing the compartment volume. At the same time, new
444 surface sites are created in the immediately adjacent compartment. Thus, the number of
445 surface sites in the simulation remains constant, but their location and therefore the
446 location of the gas-particle interface dynamically changes as material ages and
447 evaporates. The validity of this description was tested for squalane by comparing the
448 simulation results from the previously published single compartment model[9] to an
449 equivalent multi-compartment reaction-diffusion simulation using the uptake and
450 evaporation steps described above (see ESI Sec S3 and Fig. S1†). Agreement between the
451 two sets of simulations provides confidence that the interface tracking scheme accurately
452 represents how aging controls particle size and density.
453

454 *D. Model Sensitivity*

455 The extension of the reaction-diffusion scheme to include the semi-detailed free
456 radical mechanism and evaporation involves two critical assumptions. First, OH radicals
457 are assumed to react with carboxylic acids in an organic matrix with the same rate
458 coefficient as in the aqueous phase. Second, the diffusion coefficient is assumed to be
459 constant and the same everywhere in the particle despite extensive chemical changes to
460 the aerosol with oxidation. These assumptions represent two general mechanisms for
461 surface renewal in a semisolid aerosol, which can occur either by the formation of gas
462 phase reaction products (i.e. chemical erosion) or by enhanced mobility of molecules
463 (plasticization) to diffuse away from the interface into the interior of the particle. As will
464 be shown below, these two processes produce rather distinct changes in how the aerosol
465 mass and average carbon oxidation state evolve with reaction. The sensitivity of the
466 simulation predictions to these two assumptions is explicitly tested as summarized in
467 Table 2.

468 **Table 2**. Scenarios used to test the sensitivity of the model to the magnitude of the OH +
469 COOH rate coefficient $k_{OH+COOH}$ (aqueous vs. gas phase value) and diffusion. For
470 scenario 1 and 2 the diffusion coefficient (D) for all species is constant, while in 1A and
471 2A reaction products with carbon numbers (C_n) smaller than C_{16} have a higher value. See
472 text for more details.
473

Scenario	$k_{OH+COOH}$ (cm^3 molecules^{-1} s^{-1})	Diffusion coefficient (D, cm^2 s^{-1})
1	Aqueous ($k_{OH+COOH} = 10^{-14}$)[53]	Constant ($D = 8.3 \times 10^{-19}$)
2	Gas Phase ($k_{OH+COOH} = 5.2 \times 10^{-13}$)[48]	Constant ($D = 8.3 \times 10^{-19}$)
1A	Aqueous ($k_{OH+COOH} = 10^{-14}$)	$D = 8.3 \times 10^{-19}$ for $C_n \geq C_{16}$
		$D = 3.0 \times 10^{-13}$ for $C_n < C_{16}$
2A[a]	Gas Phase ($k_{OH+COOH} = 5.2 \times 10^{-13}$)	$D = 8.3 \times 10^{-19}$ for $C_n \geq C_{16}$

$D = 3.0 \times 10^{-13}$ for $C_n < C_{16}$

[a] Scenario 2A is discussed in full in ESI section 9†.

Scenario 1 assumes OH + COOH rate coefficient of 10^{-14} molecules^{-1} cm^3 s^{-1} [53] and the diffusion coefficient for all species in the simulations (reactants, products and intermediates) is 8.3×10^{-19} cm^2 s^{-1}, the value determined experimentally for pure triacontane. In Scenario 2, the rate coefficient for the OH + COOH abstraction reaction is increased to the recommended gas phase value of 5.2×10^{-13} molecules^{-1} cm^3 s^{-1},[48] while keeping the diffusion coefficients the same as in scenario 1. Because this abstraction reaction leads to fragmentation, this scenario also tests how an increase in the relative importance of fragmentation reactions impacts model predictions.

Scenario 1A extends Scenario 1 to evaluate the effect of varying diffusion coefficients due to changes in the particle composition during exposure to OH. It is likely that the formation of new oxygenated function groups on triacontane and subsequent fragmentation reactions will lead to faster diffusion either by the formation of smaller molecular weight products that plasticize the semisolid particle, or by increasing the uptake of H_2O due to increasing hygroscopicity of the aerosol.[76, 77] An analogous extension of Scenario 2 is reported in ESI Section 9†.

As described in the ESI Sec. S1†, non-Fickian or environment-sensitive diffusion paths were added to the reaction scheme to describe the plasticization process in a highly simplified way. Reaction products with 15 carbons in length or less were assumed to have a diffusion coefficient of 3×10^{-13} cm^2 s^{-1}, a factor of 4×10^5 larger than the self-diffusion coefficient of pure triacontane. This large increase in the diffusion coefficient is

496 selected somewhat arbitrarily but is the smallest change that had significant impact on the
497 overall rate of triacontane consumption, and is in the range of large decreases in viscosity
498 (and thus increased self-diffusion) observed for organic aerosols that accompany
499 relatively small changes in aerosol water content.[21, 77-80] Note that using this particular
500 model description only allows for faster diffusion in areas where lower molecular weight
501 products have been formed. Clearly a more refined description that includes diffusion
502 coefficients for all types of fragmentation products is possible, however experimental
503 data for such mixtures would be required to include the relevant absolute diffusion
504 coefficients. Absent such data, we chose the simplest possible description for this work.
505
506 **III. Simulation Results**
507 The average gas phase OH concentration in the simulation is set to be consistent
508 with experiment (2.5×10^{11} molecules cm^{-3}), leading to a maximum OH exposure of 9.3
509 $\times 10^{12}$ molecules cm^{-3} s during the 37 s residence time in the flow tube. The simulations
510 produce complete concentration vs time profiles for all species defined in the mechanism
511 as a function of compartment location. This enables the full spatial distribution of
512 products and intermediates to be viewed at any point in the reaction. To compare
513 simulation predictions for scenarios 1, 2, and 1A with experimental data, the calculated
514 mass and elemental compositions are averaged over all compartments, since the
515 experiments only contain information on how the bulk average aerosol properties evolve
516 with oxidation. Internal spatial distributions have also been extracted from the
517 calculations, and are examined below and in the ESI.

518 The simulations are compared to three main data sets. The first is the normalized
519 decay of 145 nm average diameter triacontane aerosol vs. OH exposure measured with
520 vacuum ultraviolet ionization aerosol mass spectrometry (Fig. 4) and described in detail
521 in previous publications.[29, 63] The second data set (Figs. 5-8) is the elemental composition
522 of slightly smaller 109 nm average diameter triacontane aerosol as a function of OH
523 exposure from previously published measurements[19] using an Aerodyne High Resolution
524 Mass Spectrometer with electron impact ionization. The aerosol generated from
525 semisolid triacontane is likely to be non-spherical, so a shape correction was applied to
526 the mass data as described in ESI Sec. S2.† Both the uncorrected and shape corrected
527 data are shown in Figs. 5 and 7 to illustrate the potential influence of shape.
528 Model scenarios 1 and 2, which differ only in their OH + COOH rate coefficients,
529 are plotted against the experimental data in Figs. 4-6. Scenario 1 predicts a slower loss
530 rate of triacontane (Fig. 4) than observed experimentally or predicted by Scenario 2. In
531 contrast, Scenario 1 agrees best with the measured aerosol mass in Fig. 5A but predicts
532 that the average hydrogen and carbon content in the particle are much larger than
533 observed in the experiment. Scenario 2 is only consistent with the experimental aerosol
534 mass for the first few points in Fig. 5A but predicts the average hydrogen and carbon
535 content better than Scenario 1 (Fig. 6A and B), at least up to an OH exposure of ~2 x 10^{12}
536 molec. cm^{-3} s. Beyond this exposure, Scenario 2 greatly overestimates the amount of
537 carbon removed from the particle by heterogeneous reactions. A clear deficiency in both
538 these Scenarios is the lack of new oxygenated functional groups that are formed and
539 remain in the aerosol phase as seen in Fig. 6A. This trend can also be seen in the O/C
540 and H/C elemental ratio data in Fig. 5B.

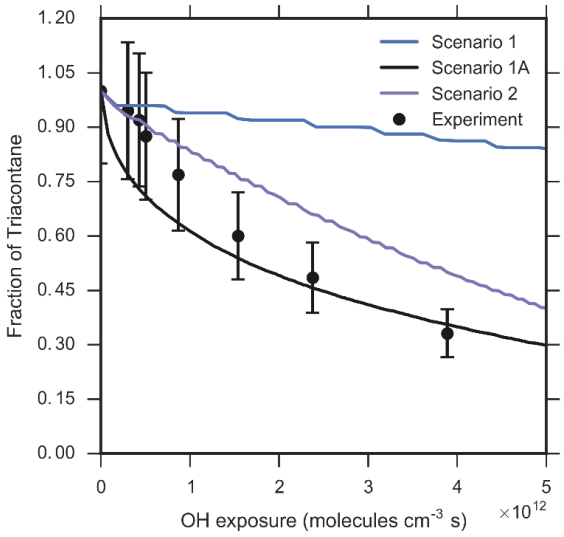

Figure 4. Experimental[29, 63] and simulated reactive decay of triacontane as function of OH exposure. Both experiment and simulation results were normalized to unreacted triacontane prior to the heterogeneous oxidation. See Table 2 for scenario descriptions. The steps seen in the Scenario 1 results are due to the representation of the system as a set of well-mixed compartments connected by very slow diffusion. They disappear when reaction and diffusion are more competitive.

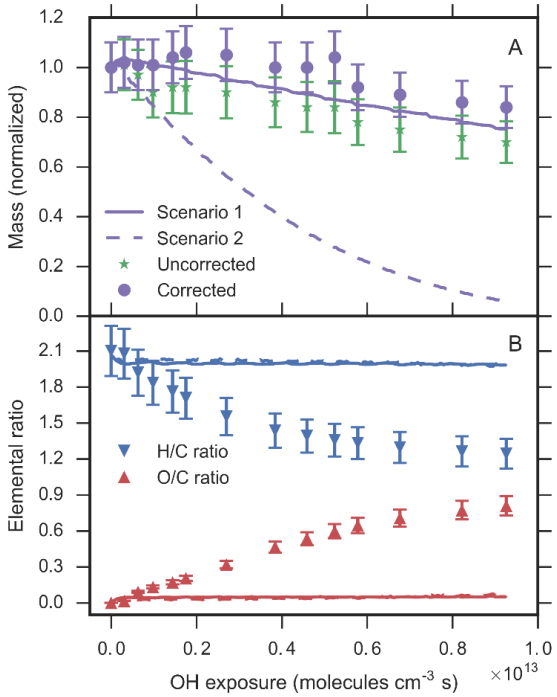

552

553 **Figure 5.** Comparison of measured (points) and simulated (lines) results using Scenarios
554 1 and 2, which evaluate sensitivity to the OH + carboxylic rate coefficient (see Table 2).
555 (A) aerosol mass; (B) H/C and O/C elemental ratios.

556

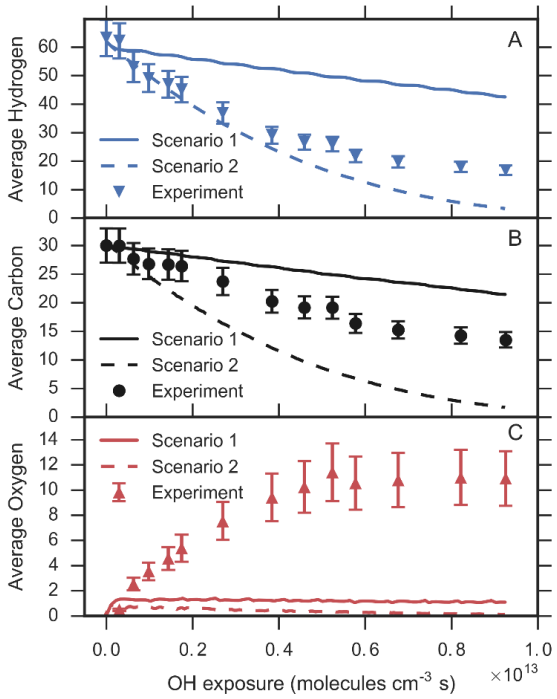

Figure 6. Average number of: (A) hydrogen, (B) carbon and (C) oxygen atoms per molecule in the aerosol as a function of OH exposure for Scenarios 1 and 2, which evaluate the model sensitivity to the OH + carboxylic rate coefficient (see Table 2).

Model Scenarios 1 and 1A and 2 and 2A (ESI Section 9) investigate the effects of an increasing self-diffusion coefficient due to plasticization. The predictions of Scenario 1A are compared to the experimental decay kinetics (Fig. 4), aerosol mass (Fig. 7A), and elemental composition (Figs. 7B and 8). There is overall agreement between Scenario 1A and the triacontane decay kinetics shown in Fig. 4, although we note that at small OH exposures Scenario 1A predicts less triacontane in the particle than is observed experimentally.

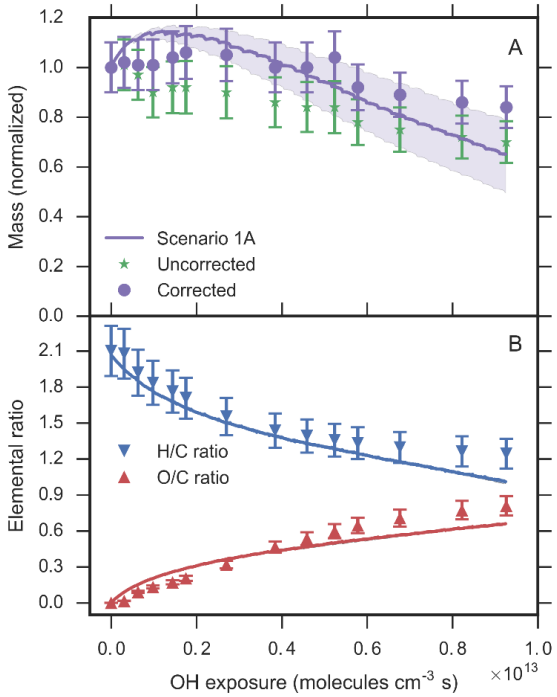

572

573 **Figure 7**. Comparison of the measured (symbols) and simulated (A) aerosol mass and (B)
574 H/C and O/C elemental ratios as a function of OH exposure for Scenario 1A, which tests
575 sensitivity to a changing self-diffusion in the aerosol due to plasticization during
576 oxidation. The shaded regions in (A) show the sensitivity of the model predictions to
577 increasing and decreasing evaporation rates by a factor of 10. This spans the uncertainty
578 in vapor pressures used in the model.
579

580

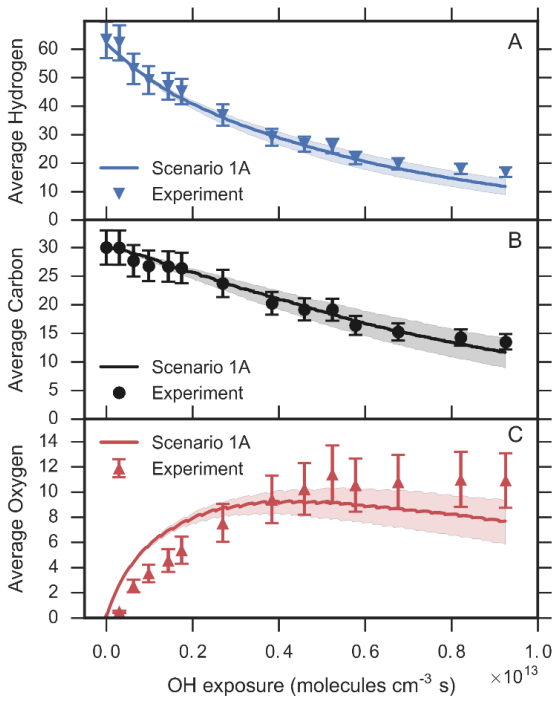

581

582 **Figure 8**. Average number of: (A) hydrogen, (B) carbon and (C) oxygen atoms in the
583 aerosol as a function of OH exposure for Scenario 1A, which tested sensitivity to
584 changing self-diffusion in the aerosol due to plasticization during oxidation. The shaded
585 regions in (A), (B) and (C) show the sensitivity of the model predictions to increasing and
586 decreasing evaporation rates by a factor of 10. This spans the uncertainty in vapor
587 pressures used in the model.
588
589

590 Scenarios 1 and 1A have somewhat similar agreement with the experimental mass
591 (cf. Fig. 5A and Fig. 7A), but the elemental composition predictions of Scenario 1A (Fig.
592 8) are in much better agreement with experiment than Scenario 1 or 2. Scenario 2A (ESI
593 Sec 9) does not show a comparable improvement to Scenario 2. Scenario 1A accurately
594 predicts the observed decrease in average hydrogen and carbon content as well as the
595 overall magnitude of the average oxygen content in the aerosol with oxidation. We note
596 some slight differences in the overall time-dependent oxygen content between scenario
597 1A and experiment. The average elemental composition predicted by Scenario 1A is in

598 good agreement with the measured H/C and O/C ratios in Fig 7B, with minor
599 discrepancies between simulation and experiment at OH exposures in excess of ~6 x 10^{12}
600 molecules cm^{-3} s. Overall, the model Scenario that best predicts the global experimental
601 data set is Scenario 1A.

602 *Spatial profiles*. Since Scenario 2 is clearly not consistent with all of the
603 experimental observations, the most useful insights for examining the internal
604 distribution of oxidized material within the aerosol can be gained by considering only
605 Scenarios 1 and 1A. As shown for Scenario 1 in Fig. 9, reaction occurs only within the
606 outermost 1 nm of the aerosol, which becomes extremely oxidized and produces a steep
607 chemical gradient in the near-surface region. A plot of the peroxy radical concentration
608 (ESI Sec. S8†, Figure S4) confirms that the reactions are confined to this region. The
609 simulations predict an O/C ratio of 1.3 at an OH exposure of 2×10^{12} molecules cm^{-3} s,
610 with some volatilization of the outer surface. At all OH exposures, the vast majority of
611 the particle remains unreacted triacontane. Volatilization of highly oxidized triacontane
612 fragments exposes less oxidized organic material, so that the particle mass and hydrogen,
613 and carbon contents all decrease without much increase in the average oxygen content.

614 Similar plots for Scenario 1A are shown in Fig. 10. In this case, the internal
615 distribution of oxidized material extends more deeply into the aerosol bulk
616 (approximately 20 nm). Fig. S5† shows that peroxy radicals are found throughout the

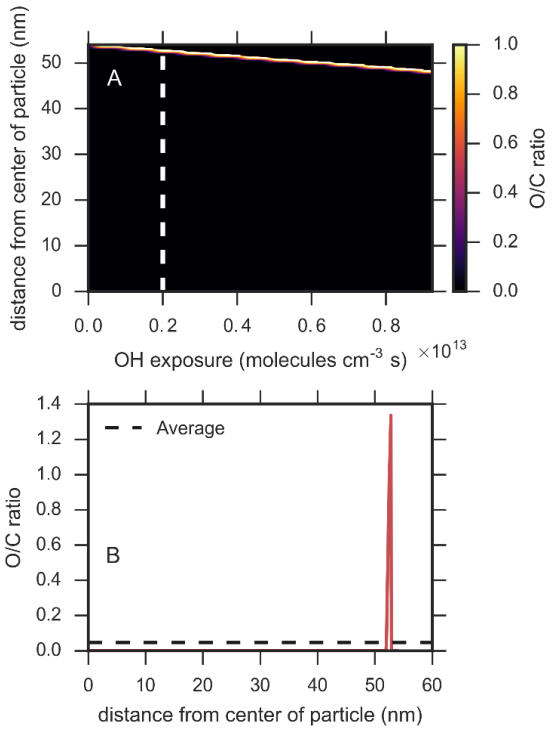

617

618 **Figure 9.** O/C ratio of the aerosol as a function of OH exposure and spatial location
619 calculated using Scenario 1. The surface of the aerosol starts at 55 nm and slowly retreats
620 along the yellow contour as material evaporates. (A) contour map of the O/C ratio. (B)
621 spatial profile at an OH exposure of 2.0×10^{12} molecules cm^{-3} s (shown as a dotted line
622 in A). The black dashed line in B corresponds to the average O/C ratio of the aerosol.
623

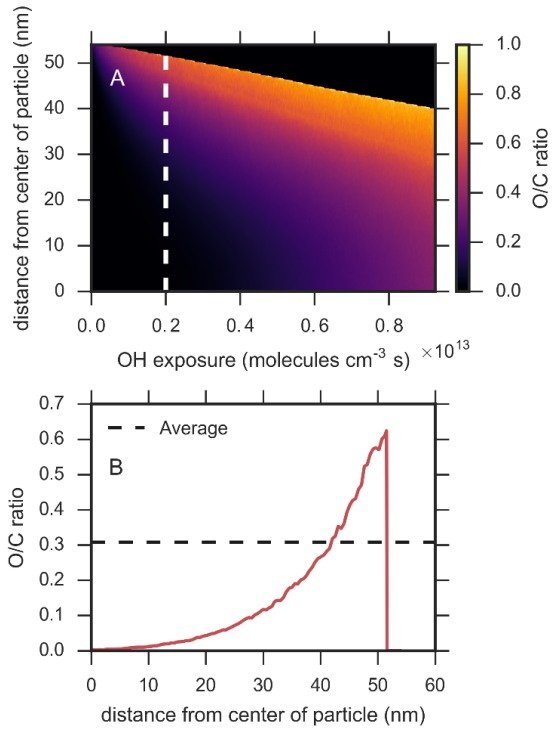

624

625

626 **Figure 10.** O/C ratio of the aerosol as a function of OH exposure and spatial location for
627 Scenario 1A. The surface of the aerosol starts at 55 nm and slowly retreats along the
628 yellow contour as material evaporates: (A) contour map of the O/C ratio. (B) Spatial
629 profile at an OH exposure of 2.0×10^{12} molecules cm^{-3} s (shown as a dotted line in A).
630 The black dashed line in B corresponds to the average O/C ratio of the aerosol.
631

632 particle, so the O/C distribution marks the location of free radical reactions., not just
633 mixing of products formed only at the surface. As shown in Fig. 10B, the aerosol
634 interface still remains more oxidized (O/C = 0.6) than the bulk at an OH exposure of $2 \times$
635 10^{12} molecules cm^{-3} and an unreacted core of starting material in the inner 10 nm. The
636 reduced extent of oxidation at the surface limits the fragmentation chemistry and
637 subsequent evaporation of volatile material from the particle.

638

639

IV. Discussion

Although Scenarios 1, 1A and 2 were constructed to evaluate key uncertainties in the model description, a deeper analysis of these predictions nevertheless provides new insights into the principles that control heterogeneous reactions of semisolid *vs* liquid aerosol. In this section we first discuss how changing a key assumption in each Scenario alters the predicted aerosol properties, followed by a detailed discussion of Scenario 1A, which accurately predicts the experimental results.

Scenarios 1, 1A, 2 and 2A. From the comparison of the Scenarios 1, 1A, 2 and 2A to the experimental results it is clear that the chemical transformation (i.e. oxidation) of triacontane by OH is not governed solely by elementary reaction pathways but depend on a number of more complex processes such as diffusion and volatilization. As seen in Fig. 4, the loss rate of triacontane itself depends sensitively upon diffusion to and from the aerosol interface, consistent with previous work on the emergent nature of reactive uptake.[6] Scenarios 1 and 1A use the same self-diffusion and OH diffusion rate coefficients (R7) for triacontane but differ in their assumption about the self-diffusion coefficient of the products, and therefore predict vastly different triacontane reaction kinetics. Therefore, there is no straightforward relationship between γ_{eff} obtained by experiment and the inherent OH reactivity of triacontane (i.e. R7). Rather, heterogeneous kinetics in semisolid aerosol is inextricably coupled with diffusion timescales, as shown previously[6], and by other surface renewal pathways as described below. This adds significant complexity to understanding the underlying principles of reactivity in semisolid aerosol compared to liquid systems.

While Scenario 1 and 1A both capture the main changes in aerosol mass with oxidation (Figs. 5A and 7A), Scenario 1 greatly under-predicts the experimentally observed oxygen content (Fig. 6C) of the aerosol and over-predicts the average hydrogen (Fig. 6A) and carbon (Fig. 6A) content remaining in the particle phase. Thus, while Scenario 1 gives a fair representation of the aerosol mass, it clear that it is for the wrong reasons. Scenario 1A alone provides a comprehensive set of predictions that capture the reaction kinetics of triacontane (Fig. 4) as well as providing an accurate description of how the elemental composition (Fig. 8) evolves to produce the observed changes in aerosol mass (Fig. 7A).

The ability of the calculations to provide spatial distributions of reactive intermediates and elemental compositions in the particles as a function of OH exposure allows identification of where the free radical chemistry occurs (see Figs 9, 10 and ESI Sec S8†). As seen in Figs 9 and S4, the slow diffusion assumption in Scenario 1 produces an aerosol with a thin highly oxidized crust (O/C = 1.3) and an interior comprised of unreacted material (O/C = 0). Once the interface is oxidized, the decay of triacontane is slow (Fig. 4) because the majority of the triacontane is diffusively confined below the interface to a region that is inaccessible to OH given its short reaction length (i.e. 1-3 nm).[6, 61] The peroxy free radicals are also confined to the interface (Fig S4) and could not propagate the reaction in the particle bulk. Thus, the slow kinetic decay predicted in Fig. 4 for Scenario 1 corresponded to the consumption of triacontane in the outermost region of the aerosol. The oxidation of this thin outer layer only produces modest changes to the average oxygen content (Fig. 6C) and elemental composition (Fig. 5B). This analysis is

684 consistent with an expanded definition of uptake[6] and with the accessible reaction volume
685 model used to interpret the heterogeneous reaction of OH with citric acid aerosol.[26]

686 The spatial composition maps for Scenario 1A (Figs. 10 and S5) clearly show that
687 the location where free radical reactions occur and the spatial distribution of the reaction
688 products (and therefore triacontane) are spread more uniformly within the aerosol,
689 although a sizable gradient in composition remains (Fig. 10B). While the self-diffusion
690 coefficient of triacontane in Scenarios 1 and 1A is the same, the enhanced mobility of
691 free radicals and reaction products (with carbon numbers less than 16) prevents the
692 formation of a semisolid oxidized crust with limited molecular mobility, thus allowing
693 oxidation to effectively access a larger fraction of the aerosol volume. This in turn leads
694 to the larger consumption rate of triacontane (Fig. 4) and the greater aerosol oxygen
695 content (Fig. 8C) observed in the experiment and predicted by Scenario 1A.

696 A comparison of Scenarios 1 and 2 indicate that additional factors beyond
697 diffusion might govern aerosol reactivity and composition. Scenarios 1 and 2 differ only
698 by the reactivity of OH with product species containing a carboxylic acid group. Scenario
699 2 uses a gas phase rate coefficient ($k_{OH+COOH}$) that is 52 times larger than aqueous phase
700 rate coefficient used in Scenario 1; otherwise the Scenarios are identical. There are
701 substantial differences between these Scenario predictions of the triacontane consumption
702 rate (Fig. 4), aerosol mass (Fig. 5) and elemental composition (Fig. 6). Scenario 2,
703 relative to 1, predicts a much faster consumption rate of triacontane with substantial loss
704 of aerosol mass, hydrogen and carbon, despite similar H/C and O/C ratios (Fig. 5). In
705 Scenario 2 the quantity of oxygen formed in the aerosol phase is much smaller in

706 Scenario 1. Addition of plasticization in Scenario 2A (ESI Sec 9†) increases the extent of
707 oxidation, but does not correctly predict the trends observed experimentally.

708 In Scenario 2, the faster consumption rate of triacontane and loss in aerosol mass
709 can be explained by the enhanced reactivity of carboxylic acids (i.e. larger $k_{OH+COOH}$).
710 The reaction of OH with -COOH forms an R(O)O radical directly, which undergoes
711 facile decomposition into CO_2 and an alkyl radical as illustrated by the right-hand branch
712 in Fig 2. This reaction pathway increases volatilization of the outer layer of the aerosol
713 via the production of CO_2, exposing unreacted triacontane below the surface and
714 promoting its reaction with OH. This also explains why smaller quantities of oxygen are
715 added to the aerosol in Scenario 2 since the lifetime of the –COOH group is ~50 times
716 smaller than in Scenario 1.

717 It is clear from the analysis above that the oxidation rate and elemental
718 composition of this semisolid aerosol is governed by additional processes that are not
719 present in liquid aerosol systems. One central factor governing the reactivity of semisolid
720 systems is mechanism and timescale for molecules beneath the interface to access the
721 surface and undergo reaction with OH. This is in contrast with results for a liquid aerosol
722 (squalane), which was observed to be internally well-mixed between reactive OH
723 collisions under similar reaction conditions to those used for triacontane.[6] For
724 triacontane, species can access the surface region either by enhanced product diffusion or
725 by chemical erosion. Both of these processes, albeit in different ways, prevent the
726 formation of a stable 1-3 nm thick highly oxidized low mobility layer (observed in
727 Scenario 1, Fig. 9) that would otherwise diffusively confine triacontane and chemically
728 deactivate it in the interior of the aerosol. The key differences between these two

729 processes have to do with their effect on the average carbon oxidation state of the aerosol
730 phase. Enhanced diffusion (Scenario 1A) increases the average bulk aerosol carbon
731 oxidation state whereas chemical erosion (Scenario 2) leaves the particle chemically
732 reduced, instead forming highly oxidized gas phase reaction products (i.e. CO_2). For
733 triacontane, surface renewal and consumption of the starting material appears to be
734 driven mainly by diffusion, leading to the sizable increase in the average oxygen content
735 of the aerosol observed by experiment and accurately predicted by Scenario 1A. In
736 general, exactly how and if surface renewal occurs in semisolid or glassy aerosol could
737 depend sensitively upon the aerosol composition, water content and oxidant
738 concentration. An example of the importance of composition is found in mechanistic
739 studies of ozone oxidation of oleic acid and related olefinic compounds that have been
740 reported in the literature.[78, 81] For these molecules, the C=C double bond opens free
741 radical addition reaction channels leading to oligomerization that do not exist in
742 aliphatics such as squalane and triacontane. Experiments and models indicate that
743 oligomerization does occur, and that there is stiffening rather than plasticization of the
744 aerosol matrix during oxidation when olefins are present. There can be a counteracting
745 plasticization when water is present.[10]

746 *Scenario 1A.* The semi-detailed reaction-diffusion reaction scheme developed for
747 oxidation of triacontane, a semisolid aliphatic aerosol, is an expansion of the previously
748 reported single compartment (instantaneously mixed) mechanism that successfully
749 predicted the elemental composition, mass, and effective uptake for the reaction of
750 squalane with OH radicals.[6, 9] Inclusion of additional reaction steps is required because
751 the diffusive confinement of free radical intermediates near the particle surface results in

752 a much greater degree of oxidation than for a liquid system (i.e. squalane) under
753 comparable OH exposure conditions. The major elements added are chemical reactions
754 for the formation and destruction of carboxylic acids, fragmentation of carbon backbones
755 of all lengths, not just the 30-carbon backbone, and full diffusion of all species.

756 Predictions from Scenario 1A describe the global data set well and allow us to
757 more closely examine the underlying oxidation mechanism. Although the free radical
758 chemistry can proceed via numerous parallel pathways, we find that in the triacontane
759 system one major intermediate species dominates the chemistry. Triacontane molecules
760 and their oxidation products consist of primary and secondary C-H bonds with a terminal
761 methyl group oriented toward the outer surface of the particle.[46, 71] Abstraction of a
762 primary hydrogen leads to a sequence of steps forming primary RO_2 radicals, aldehydes,
763 $R(O)O_2$ radicals, and carboxylic acids, as shown in the box in Fig. 11. Also shown in Fig
764 11 is the abstraction of secondary hydrogen atoms forming peroxy radicals, which can
765 react to form stable, chain terminating ketones or alkoxy radicals that fragment to form a
766 primary radical, thus feeding directly into the primary H abstraction product sequence.
767 While ketones from the secondary C-H branch are relatively unreactive, the primary
768 aldehydes are highly reactive towards OH,[48] and hydrogen abstraction from the -CHO
769 moiety is a significant driver of fragmentation and volatilization in this system. The
770 formation of appreciable quantities of fragmentation products in the near-surface region
771 of the particle occurs early in the OH exposure process, as shown in Fig 12. The
772 distribution is predicted to be nearly monodisperse across chain lengths once triacontane
773 begins to decompose.

This is in contrast with our previous study on squalane, where the reactions are dominated by H atoms located at tertiary and secondary carbon sites on the molecule since the reaction of primary hydrogens on the methyl groups of squalane was found to be kinetically insignificant.[9] While ketones are the primary reaction products for both squalane and triacontane (Fig. 13), the coupling of aldehyde and carboxylic acid

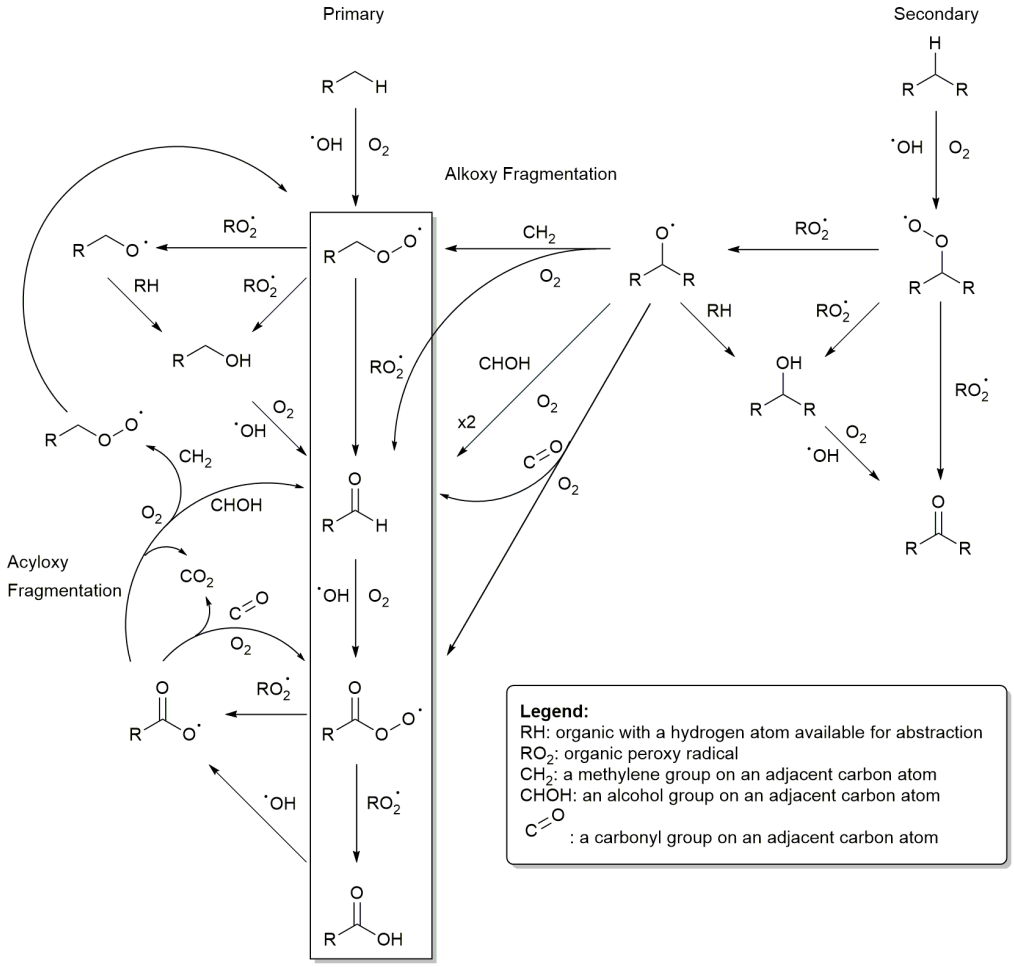

Figure 11. A schematic representation of the half-reactions involved in the free radical chemistry used to model the heterogeneous oxidation of organic aerosol by OH radicals. For a semi-solid linear alkane like triacontane, the functionalization and fragmentation free radical chemistry originates from the sequential formation of primary peroxy radicals, aldehydes, acylperoxy radicals, and acids (identified in the box). The fragmentation of primary alkoxy radicals and the formation of alkyl radicals from alkoxy hydrogen abstraction reactions are included in the model but these steps are not shown for clarity.

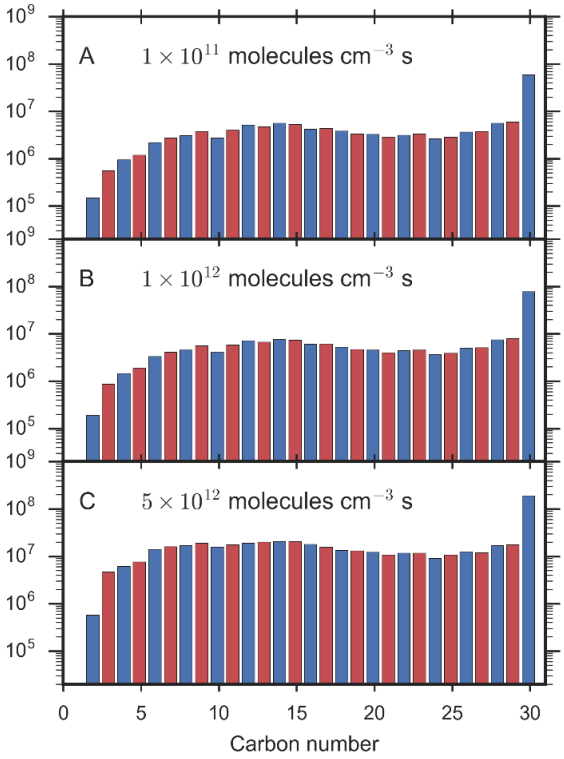

Figure 12. Carbon chain fragment distribution in the top 5 nm of the triacontane particle at 3 different OH exposure times at an OH density of 2.5 x 10^{11} molecules cm^{-3}, Scenario 1A (A) after 0.4 sec; (B) after 4 sec; and (C) after 20 sec. The increase in C_{30} with time reflects the effective roughening of the particle surface (i.e. spreading of the interface region over several compartments) as the triacontane erodes.

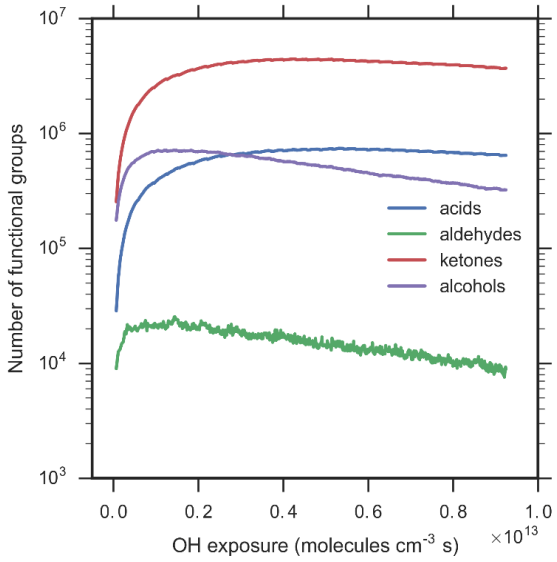

798

799 **Figure 13.** Evolution of the distribution of functional groups present in a
800 triacontane particle as a function of OH exposure, predicted using Scenario 1A. The low
801 concentration of aldehydes relative to the other functional groups is consistent with its
802 consumption as a major intermediate in the free radical chain reaction.
803

804 chemistry shown in Fig. 11 was not observed to be significant in squalane.[9] These
805 differences arise mainly from the difference in reactive sites between squalane and
806 triacontane (linear vs. branched alkane) and surface orientation, which promotes
807 abstraction from the methyl groups on triacontane and aldehyde formation. Finally, the
808 decrease in aerosol mass in the squalane system is driven by the formation and
809 subsequent decomposition of activated alkoxy radicals rather than for example CO_2
810 production from acyloxy fragmentation in triacontane.

811 *Implications for atmospheric aging of semisolid aerosol.* Although the alkane/OH
812 oxidation reaction used in this study reveals many of the fundamental transformation
813 processes expected in the atmospheric aging of ambient aerosol, it certainly lacks the
814 immense chemical complexity of SOA, which is comprised of multifunctional highly
815 oxidized molecules with smaller carbon numbers. Despite this difference,

multigenerational oxidation of triacontane forms a highly oxidized crust (O/C ~0.6-1.2) and ensuing free radical pathways (e.g. activated alkoxy decomposition) could in fact be a quite reasonable analog for the surfaces of secondary organic aerosols. However, a key difference remains in the composition, chemistry, hygroscopicity, and diffusion of material beneath this crust. For SOA, this material is expected to be much more oxidized than triacontane, with differences expected in the rate of water diffusion, for example. We also note that previous studies examining heterogeneous ozonolysis[78, 81] observed particle phase chemical gradients due to a slowing of diffusion upon oxidation, presumably due to oligomer formation, which is not an important pathway for OH initiated oxidative aging of alkanes.

Nevertheless, the large internal gradients of oxidized material in semi-solid organic aerosol observed here may have important implications for both aerosol hygroscopicity and optical properties if present under atmospheric conditions. The average O/C ratio of an aerosol has been correlated with hygroscopicity to find simplified relationships between composition and cloud condensation nuclei (CCN) activity and hygroscopic growth.[48, 82, 83] The enhanced concentrations of hydrophilic functional groups predicted to be present at the surface of a semisolid particle may increase the CCN activity or hygroscopicity relative to the value expected from the average O/C ratio. This has been suggested as an explanation for results of CCN measurements of 4-methyl-5-nitrocatechol semisolid organic aerosols aged by OH radicals, which show an enhancement in hygroscopicity after an OH exposure of 4×10^{11} molecules cm^{-3} s despite the small change in O/C ratio.[76] As predicted in this work, similar effects could occur in aliphatic systems such as triacontane since the products at the surface include

839 hygroscopic species such as small-chain dicarboxylic acids.[84, 85] The retention of water
840 molecules formed by hydrogen abstraction by OH radicals and increasing uptake of water
841 from the gas phase in the flow tube reactor may occur at the later stages of oxidation.
842 Because of the lack of direct experimental information on water concentrations in the
843 aerosol and the generally hydrophobic character of the triacontane surface under the
844 simulated conditions, water was not explicitly included in the reaction scheme used in
845 this work. Water accumulation from these processes could be partly responsible for the
846 plasticization of the outer layers of the aerosol, however. The chemical gradients in the
847 aerosol may also influence the interactions of the aerosol with light since the optical
848 properties may be similar to an aerosol with core-shell morphology.[86]

849 The findings at an OH density in the range of $\approx 10^{11}$ molecules cm^{-3} may not
850 directly extrapolate to atmospheric conditions, however, because diffusion rates can be
851 competitive with rare oxidation events, and the steep gradients predicted here may not be
852 maintained.[6] In order to test this possibility, the oxidation of triacontane was simulated
853 for 2 cases, Scenarios 1 and 1A, using an OH concentration of 5×10^6 molecules cm^{-3}
854 and a total OH exposure of 2×10^{12} molecules cm^{-3} s^{-1} (a total continuous reaction time
855 of 4.6 days). Fig. 14 shows the internal distribution of the O/C ratio found for Scenario 1.
856 Despite the increase in mixing time relative to OH uptake, chemical gradients still form
857 after oxidative aging, consistent with previous predictions for the homogeneity of a
858 particle of this size and self-diffusion coefficient.[6] If there is no plasticization when
859 oxidation is slow, even apparently slow heterogeneous aging by OH radicals can oxidize
860 the surface quite extensively compared to the change in the average chemical properties
861 and thus can affect the hygroscopicity and optical properties of the aerosol. If

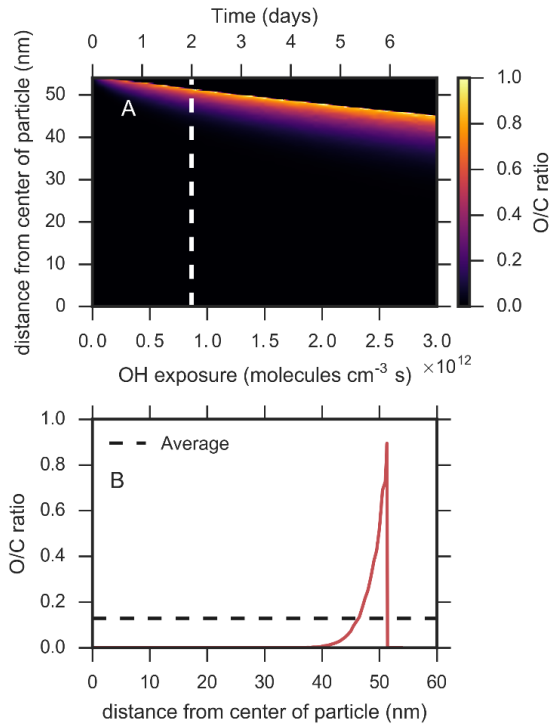

862 **Figure 14**. Internal distribution of O/C ratio of the aerosol in Scenario 1 simulated using
863 atmospheric [OH] = 5×10^6 molecules cm^{-3}. The surface of the aerosol starts at 55 nm
864 and slowly retreats along the green contour as material evaporates. (A) contour map of
865 the O/C ratio. (B) spatial profile at an OH exposure of 2.0×10^{12} molecules cm^{-3} s
866 (shown as a dotted line in A). The black dashed line in B corresponds to the average O/C
867 ratio of the aerosol.
868

869 plasticization does occur under atmospheric conditions as in Scenario 1A, (Fig. 15)
870 however, the aerosol will behave in a liquid-like manner despite its semi-solid nature,
871 appearing to be well-mixed at all times. This is consistent with trends predicted in our
872 study of emergent effects in reactive uptake.[6]

873
874
875
876
877
878

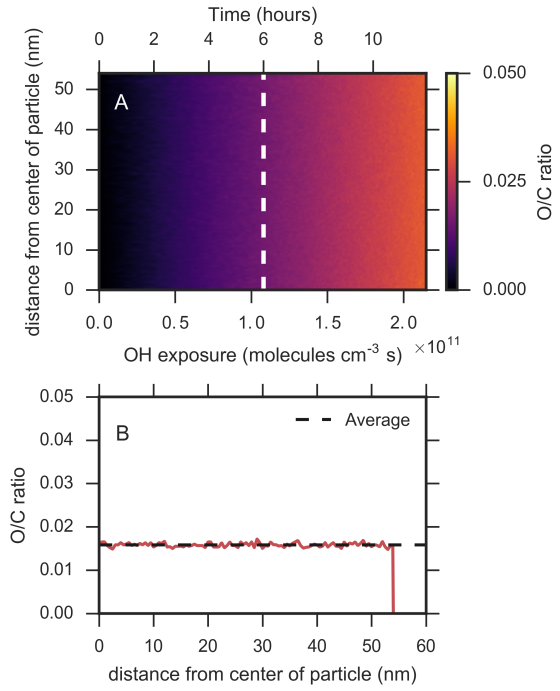

Figure 15. Internal distribution of O/C ratio of the aerosol in Scenario 1A at the end of 12 hours, simulated using atmospheric [OH] = 5×10^6 molecules cm^{-3}. Minimal volume loss is predicted at this short time, and the aerosol is well mixed. (A) contour map of the O/C ratio. (B) spatial profile at an OH exposure of 1.1×10^{11} molecules cm^{-3} s (shown as a dotted line in A). The black dashed line in B corresponds to the average O/C ratio of the aerosol.

It should be noted that inclusion of OH chemistry only is not a complete picture of oxidative ageing in the atmosphere: additional chemistries should also be taken into account in predictions of how semi-solid aerosol evolve. Reactions that could be added include RO_2 + RH,[87] HO_2 + RO_2,[52] NO + RO_2,[64, 88] and SO_2 + RO_2.[65] These reactions may become important under atmospheric conditions because the low RO_2 concentrations suppress bimolecular RO_2+RO_2 reactions, leading to a longer chemical lifetime for RO_2.

Since most of these reactions are oxidizing,[64, 65, 87] their inclusion might intensify any chemical gradients that form. Thus, the physical state of chemically aged organic aerosols under atmospheric conditions is uncertain, and additional experimental and model studies are warranted to investigate under which conditions chemical gradients form and are maintained.

Conclusions

Studies of oxidation of model organic aerosol systems provide a useful platform to understand not only processes that occur in the atmosphere but also deeper principles of reaction in confined spaces. In this work, the effect of viscosity on reactivity has been examined by constructing a semi-detailed chemical kinetics model of the heterogeneous oxidation of a semisolid C_{30} organic aerosol, triacontane, by OH radicals. The model is an extension of the schemes used for simulation of liquid-phase oxidation of a C_{30} aerosol, squalane, in prior studies. Certain elements of the chemical kinetics have not been well-studied, however, so Scenarios examining ranges of values have been constructed to evaluate the impact of 2 core assumptions. The reaction-diffusion scheme is physically based therefore it produces an absolute time base that can be used to compare the results directly to experiment. The simulations of triacontane oxidation under these Scenarios all show that under flow tube conditions, large chemical gradients in oxidized materials form, resulting in a surface that is far more oxidized than would be expected from measurements of the bulk average O/C ratio. Of the several tested, the only Scenario that reproduces the experimental data is one that includeds an increase in the self-diffusion coefficient after $<C_{16}$ products form, i.e., the near-surface region of the

920 particle becomes plasticized during the oxidation process. The successful use of a single
921 set of kinetic parameters to model the oxidation of squalane (liquid) and triacontane
922 (semi-solid) demonstrates that the proposed reaction scheme is both predictive and
923 general for aliphatic hydrocarbons. Additional extensions to this scheme are
924 straightforward to implement, and could include reactions of alkene, cyclic, and aromatic
925 moieties as well as other gas-phase reactants besides OH.

926 Examination of trends in the scenario predictions enables some specific elements
927 controlling reactivity to be identified. Viscosity has a major effect, controlling the
928 location of the oxidation reactions through diffusive confinement. More subtly, it also
929 affects the extent of oxidation, the nature of the products formed, and balance between
930 reaction and evaporation. Although the free radical chain reactions that are launched form
931 a complex web, the simulation results show that one particular branch of the chemistry,
932 reactions of aldehydes, controls the fragmentation and eventual volatilization processes in
933 the semisolid material. This specificity is not observed for the same chemistry in a liquid.

934 Because the reaction-diffusion scheme is predictive, it can be used to examine the
935 chemical processes the model aerosols would undergo if exposed to OH at a density
936 typical of that in the atmosphere. The simulations show that chemical gradients may form
937 under atmospheric conditions if there is no plasticization, but the oxidizing particle is
938 well-mixed (liquid-like) with plasticization. These predictions are consistent with a
939 previous study that showed the role of viscosity is determined by the mobility of species
940 in the particle relative to the OH reactive collision frequency.[6] Whether or not
941 plasticization is important when collisions are rare should be explicitly evaluated. The
942 possibility that chemical gradients form under these conditions has important

943 implications for both the hygroscopicity and the optical properties of the aerosol since
944 both depend on the chemical composition of the surface of the aerosol.
945
946 **Acknowledgements**
947 This material is based upon work supported by the Laboratory Directed Research and
948 Development Program of the Department of Energy's Lawrence Berkeley National
949 Laboratory under U.S. Department of Energy Office of Science, Office of Basic Energy
950 Sciences under Contract No. DE-AC02-05CH11231. Results were used from past K. R.
951 W. work supported by the Department of Energy's Office of Science Early Career
952 Research Program and by Chemical Sciences Division of the U.S. Department of Energy
953 under Contract No. DE-AC02-05CH11231. W. D. H. is supported by CHTC. The authors
954 are grateful to Prof. Jesse Kroll (MIT) and Christopher Lim (MIT) for their assistance
955 with the experimental data.
956
957
958 **References**
959 1. S. E. Schwartz and J. E. Freiberg, *Atmos Environ*, 1981, **15**, 1129-1144.
960 2. G. D. Smith, E. Woods, T. Baer and R. E. Miller, *J Phys Chem A*, 2003, **107**,
961 9582-9587.
962 3. R. A. Zaveri, R. C. Easter, J. E. Shilling and J. H. Seinfeld, *Atmos Chem Phys*,
963 2014, **14**, 5153-5181.
964 4. B. Zobrist, V. Soonsin, B. P. Luo, U. K. Krieger, C. Marcolli, T. Peter and T.
965 Koop, *Phys Chem Chem Phys*, 2011, **13**, 3514-3526.
966 5. M. Shiraiwa, C. Pfrang, T. Koop and U. Pöschl, *Atmos Chem Phys*, 2012, **12**,
967 2777-2794.

6. F. A. Houle, W. D. Hinsberg and K. R. Wilson, *Phys. Chem. Chem. Phys.*, 2015, **17**, 4412-4423.

7. M. E. Jenkin, S. M. Saunders and M. J. Pilling, *Atmos Environ*, 1997, **31**, 81-104.

8. P. Roldin, A. C. Eriksson, E. Z. Nordin, E. Hermansson, D. Mogensen, A. Rusanen, M. Boy, E. Swietlicki, B. Svenningsson, A. Zelenyuk and J. Pagels, *Atmos Chem Phys*, 2014, **14**, 7953-7993.

9. A. A. Wiegel, K. R. Wilson, W. D. Hinsberg and F. A. Houle, *Phys. Chem. Chem. Phys.*, 2015, **17**, 4398-4411.

10. T. Berkemeier, S. S. Steimer, U. K. Krieger, T. Peter, U. Poschl, M. Ammann and M. Shiraiwa, *Phys Chem Chem Phys*, 2016, **18**, 12662-12674.

11. N. A. Hosny, C. Fitzgerald, A. Vysniauskas, A. Athanasiadis, T. Berkemeier, N. Uygur, U. Poschl, M. Shiraiwa, M. Kalberer, F. D. Pope and M. K. Kuimova, *Chem Sci*, 2016, **7**, 1357-1367.

12. R. M. Bain, C. J. Pulliam and R. G. Cooks, *Chem Sci*, 2015, **6**, 397-401.

13. A. Fallah-Araghi, K. Meguellati, J.-C. Baret, A. E. Harrak, T. Mangeat, M. Karplus, S. Ladame, C. M. Marques and A. D. Griffiths, *Physical Review Letters*, 2014, **112**, 028301.

14. M. Girod, E. Moyano, D. I. Campbell and R. G. Cooks, *Chem Sci*, 2011, **2**, 501-510.

15. J. K. Lee, S. Banerjee, H. G. Nam and R. N. Zare, *Quarterly Reviews of Biophysics*, 2015, **48**, 437-444.

16. J. K. Lee, S. Kim, H. G. Nam and R. N. Zare, *Proceedings of the National Academy of Sciences*, 2015, **112**, 3898-3903.

17. T. Müller, A. Badu-Tawiah and R. G. Cooks, *Angewandte Chemie International Edition*, 2012, **51**, 11832-11835.

18. Q. Zhang, X.-Z. Shu, J. M. Lucas, F. D. Toste, G. A. Somorjai and A. P. Alivisatos, *Nano Letters*, 2014, **14**, 379-383.

19. J. H. Kroll, C. Y. Lim, S. H. Kessler and K. R. Wilson, *J Phys Chem A*, 2015, **119**, 10767-10783.

20. C. D. Cappa and K. R. Wilson, *Atmos Chem Phys*, 2011, **11**, 1895-1911.

21. L. Renbaum-Wolff, J. W. Grayson, A. P. Bateman, M. Kuwata, M. Sellier, B. J. Murray, J. E. Shilling, S. T. Martin and A. K. Bertram, *Proceedings of the*

National Academy of Sciences of the United States of America, 2013, **110**, 8014-8019.

22. T. D. Vaden, D. Imre, J. Beránek, M. Shrivastava and A. Zelenyuk, *Proceedings of the National Academy of Sciences of the United States of America*, 2011, DOI: 10.1073/pnas.1013391108.

23. A. Virtanen, J. Joutsensaari, T. Koop, J. Kannosto, P. Yli-Pirilä, J. Leskinen, J. M. Mäkelä, J. K. Holopainen, U. Pöschl, M. Kulmala, D. R. Worsnop and A. Laaksonen, *Nature*, 2010, **467**, 824-827.

24. B. Zobrist, C. Marcolli, D. A. Pedernera and T. Koop, *Atmos Chem Phys*, 2008, **8**, 5221-5244.

25. A. M. Arangio, J. H. Slade, T. Berkemeier, U. Pöschl, D. A. Knopf and M. Shiraiwa, *The Journal of Physical Chemistry A*, 2015, **119**, 4533-4544.

26. J. F. Davies and K. R. Wilson, *Chem. Sci.*, 2015, **6**, 7020-7027.

27. M. Shiraiwa, M. Ammann, T. Koop and U. Pöschl, *Proceedings of the National Academy of Sciences of the United States of America*, 2011, **108**, 11003-11008.

28. D. L. Bones, J. P. Reid, D. M. Lienhard and U. K. Krieger, *Proceedings of the National Academy of Sciences of the United States of America*, 2012, **109**, 11613-11618.

29. J. D. Smith, J. H. Kroll, C. D. Cappa, D. L. Che, C. L. Liu, M. Ahmed, S. R. Leone, D. R. Worsnop and K. R. Wilson, *Atmos Chem Phys*, 2009, **9**, 3209-3222.

30. X. Zhang and J. H. Seinfeld, *Atmos Chem Phys*, 2013, **13**, 5907-5926.

31. C. D. Cappa and K. R. Wilson, *Atmos. Chem. Phys.*, 2012, **12**, 9505-9528.

32. F. A. Houle, W. D. Hinsberg and M. I. Sanchez, *Macromolecules*, 2002, **35**, 8591-8600.

33. R. Atkinson, *Atmos Environ*, 2007, **41**, 8468-8485.

34. J. H. Kroll, J. D. Smith, D. L. Che, S. H. Kessler, D. R. Worsnop and K. R. Wilson, *Physical chemistry chemical physics : PCCP*, 2009, **11**, 7759.

35. P. A. J. Bagot, C. Waring, M. L. Costen and K. G. McKendrick, *The Journal of Physical Chemistry C*, 2008, **112**, 10868-10877.

36. G. M. Nathanson, *Annual Review of Physical Chemistry*, 2004, **55**, 231-255.

37. J. H. Kroll, N. M. Donahue, J. L. Jimenez, S. H. Kessler, M. R. Canagaratna, K. R. Wilson, K. E. Altieri, L. R. Mazzoleni, A. S. Wozniak, H. Bluhm, E. R.

Mysak, J. D. Smith, C. E. Kolb and D. R. Worsnop, *Nature chemistry*, 2011, **3**, 133-139.

38. L. H. Renbaum and G. D. Smith, *Phys Chem Chem Phys*, 2009, **11**, 2441-2451.

39. W. D. Hinsberg and F. A. Houle, Kinetiscope: (http://hinsberg.net/kinetiscope/).

40. D. Bunker, B. Garrett, T. Kleindienst and G. L. III, *Combustion and Flame*, 1974, **23**, 373-379.

41. D. T. Gillespie, *J Comput Phys*, 1976, **22**, 403-434.

42. F. A. Houle, W. D. Hinsberg, M. Morrison, M. I. Sanchez, G. Wallraff, C. Larson and J. Hoffnagle, *Journal of Vacuum Science & Technology B: Microelectronics and Nanometer Structures*, 2000, **18**, 1874.

43. G. Wallraff, J. Hutchinson, W. Hinsberg, F. Houle, P. Seidel, R. Johnson and W. Oldham, *Journal of Vacuum Science & Technology B: Microelectronics and Nanometer Structures*, 1994, **12**, 3857.

44. F. A. Houle, W. D. Hinsberg, M. I. Sanchez and J. A. Hoffnagle, *J Vac Sci Technol B*, 2002, **20**, 924-931.

45. M. H. Cohen and D. Turnbull, *The Journal of Chemical Physics*, 1959, **31**, 1164-1169.

46. C. R. Ruehl, T. Nah, G. Isaacman, D. R. Worton, A. W. H. Chan, K. R. Kolesar, C. D. Cappa, A. H. Goldstein and K. R. Wilson, *The journal of physical chemistry. A*, 2013, **117**, 3990-4000.

47. J. Vieceli, M. Roeselova, N. Potter, L. X. Dang, B. C. Garrett and D. J. Tobias, *The journal of physical chemistry. B*, 2005, **109**, 15876-15892.

48. E. S. C. Kwok and R. Atkinson, *Atmos Environ*, 1995, **29**, 1685-1695.

49. H. Zhang, C. R. Ruehl, A. W. H. Chan, T. Nah, D. R. Worton, G. Isaacman, A. H. Goldstein and K. R. Wilson, *J Phys Chem A*, 2013, **117**, 12449-12458.

50. E. T. Denisov and I. B. Afanas'ev, *Oxidation and Antioxidants in Organic Chemistry and Biology*, Boca Raton, FL, 2005.

51. E. Villenave, R. Lesclaux, S. Seefeld and W. R. Stockwell, *Journal of Geophysical Research*, 1998, **103**, 25273.

52. J. J. Orlando and G. S. Tyndall, *Chemical Society reviews*, 2012, **41**, 6294-6317.

53. G. V. Buxton, C. L. Greenstock, W. P. Helman, A. B. Ross and W. Tsang, *Journal of Physical and Chemical Reference Data*, 1988, **17**, 513-886.

54. B. Ervens, S. Gligorovski and H. Herrmann, *Phys Chem Chem Phys*, 2003, **5**, 1811-1824.

55. N. K. Vel Leitner and M. Doré, *Water Research*, 1997, **31**, 1383-1397.

56. T. J. Dillon and J. N. Crowley, *Atmos Chem Phys*, 2008, **8**, 4877-4889.

57. C. B. M. Gross, T. J. Dillon, G. Schuster, J. Lelieveld and J. N. Crowley, *The journal of physical chemistry. A*, 2014, **118**, 974-985.

58. J. B. S. Burkholder, S. P.; Abbatt, J.; Barker, J. R.; Huie, R. E.; Kolb, C. E.; Kurylo, M. J.; Orkin, V. L.; Wilmouth, D. M.; Wine, P. H. , *JPL Publication 15-10, Jet Propulsion Laboratory, Pasadena, CA*, 2015, http://jpldataeval.jpl.nasa.gov.

59. P. S. J. Lakey, I. George, L. Whalley, M. T. Baeza-Romero and D. E. Heard, *Environmental Science & Technology*, 2015, **49**, 4878-4885.

60. L. Vereecken and J. Peeters, *Physical chemistry chemical physics : PCCP*, 2009, **11**, 9062-9074.

61. L. Lee and K. Wilson, *The Journal of Physical Chemistry A*, 2016, **120**, 6800-6812.

62. J. H. Slade and D. A. Knopf, *Geophysical Research Letters*, 2014, **41**, 5297-5306.

63. C.-L. Liu, J. D. Smith, D. L. Che, M. Ahmed, S. R. Leone and K. R. Wilson, *Phys Chem Chem Phys*, 2011, **13**, 8993-9007.

64. N. K. Richards-Henderson, A. H. Goldstein and K. R. Wilson, *The Journal of Physical Chemistry Letters*, 2015, **6**, 4451-4455.

65. N. K. Richards-Henderson, A. H. Goldstein and K. R. Wilson, *Environmental Science and Technology*, 2016, **50**, 3554-3561.

66. M. Ammann, U. Poschl and Y. Rudich, *Phys Chem Chem Phys*, 2003, **5**, 351-356.

67. R. Atkinson, *Atmos. Chem. Phys.*, 2003, **3**, 2233-2307.

68. B. M. Ocko, X. Z. Wu, E. B. Sirota, S. K. Sinha, O. Gang and M. Deutsch, *Physical Review E*, 1997, **55**, 3164-3182.

69. S. Fujiwara and T. Sato, *The Journal of Chemical Physics*, 1999, **110**, 9757-9764.

70. H. Z. Li and T. Yamamoto, *Journal of the Physical Society of Japan*, 2002, **71**, 1083-1090.

71. H. Zhang, D. R. Worton, S. Shen, T. Nah, G. Isaacman-VanWertz, K. R. Wilson and A. H. Goldstein, *Environmental Science & Technology*, 2015, **49**, 9768-9777.

72. S. Compernolle, K. Ceulemans, J.-F. Müller and J. F. M̈uller, *Atmos Chem Phys*, 2011, **11**, 8385-8394.

73. V. Soonsin, A. A. Zardini, C. Marcolli, A. Zuend and U. K. Krieger, *Atmos Chem Phys*, 2010, **10**, 11753-11767.

74. S. Compernolle, K. Ceulemans and J. F. Müller, *Atmos Chem Phys*, 2011, **11**, 9431-9450.

75. A. Bondi, *The Journal of Physical Chemistry*, 1964, **68**, 441-451.

76. J. H. Slade, R. Thalman, J. Wang and D. A. Knopf, *Atmos Chem Phys*, 2015, **15**, 10183-10201.

77. Y. Zhang, M. S. Sanchez, C. Douet, Y. Wang, A. P. Bateman, Z. Gong, M. Kuwata, L. Renbaum-Wolff, B. B. Sato, P. F. Liu, A. K. Bertram, F. M. Geiger and S. T. Martin, *Atmos Chem Phys*, 2015, **15**, 7819-7829.

78. N. A. Hosny, C. Fitzgerald, A. Vysniauskas, T. Athanasiadis, T. Berkemeier, N. Uygur, U. Pöschl, M. Shiraiwa, M. Kalberer, F. D. Pope and M. K. Kuimova, *Chem. Sci.*, 2016, **7**, 1357-1367.

79. F. H. Marshall, R. E. H. Miles, Y.-c. Song, P. B. Ohm, R. M. Power, J. P. Reid and C. S. Dutcher, *Chem. Sci.*, 2016, **7**, 1298-1308.

80. R. M. Power, S. H. Simpson, J. P. Reid and a. J. Hudson, *Chem Sci*, 2013, **4**, 2597.

81. C. Pfrang, M. Shiraiwa and U. Poschl, *Atmos Chem Phys*, 2011, **11**, 7343-7354.

82. M. Petters, H. Wex, C. Carrico, E. Hallbauer, A. Massling, G. McMeeking, L. Poulain, Z. Wu, S. Kreindenweis and F. Stratmann, *Atmos Chem Phys*, 2009, **9**, 3999-4009.

83. M. D. Petters and S. M. Kreidenweis, *Atmos Chem Phys*, 2007, **7**, 1961-1971.

84. C. R. Ruehl, J. F. Davies and K. R. Wilson, *Science*, 2016, **351**, 1447-1450.

85. C. R. Ruehl and K. R. Wilson, *The journal of physical chemistry. A*, 2014, **118**, 3952-3966.

86. S. Ramachandran and R. Srivastava, *Environmental Science: Processes & Impacts*, 2013, **15**, 1070-1077.

87. J. D. Crounse, L. B. Nielsen, S. Jørgensen, H. G. Kjaergaard and P. O. Wennberg, *The Journal of Physical Chemistry Letters*, 2013, **4**, 3513-3520.

88. L. H. Renbaum and G. D. Smith, *Phys Chem Chem Phys*, 2009, **11**, 8040.